



Mechanics and deformation of shape memory polymer kirigami microstructures



Kian Bashandeh^a, Jungkyu Lee^b, Qian Wu^c, Yi Li^d, Xueju Wang^d, Yan Shi^{c,1}, Xiaogang Guo^e, Yonggang Huang^f, John A. Rogers^g, Andreas A. Polycarpou^{a,*}

^a Department of Mechanical Engineering, College of Engineering, Texas A&M University, College Station, 77843-3123, TX, USA

^b Bruker Nano Surfaces, Eden Prairie, MN 55344, USA

^c State Key Laboratory of Mechanics and Control of Mechanical Structures, Nanjing University of Aeronautics and Astronautics, Nanjing, 210016, China

^d Department of Mechanical and Aerospace Engineering, University of Missouri–Columbia, Columbia, MO 65211, USA

^e Yuhang Building, Beijing Institute of Technology, 5 South Zhongguancun Street, Haidian District, Beijing, 100081, China

^f Departments of Mechanical Engineering and Civil and Environmental Engineering, Northwestern University, Evanston, IL 60208, USA

^g Departments of Materials Science and Engineering, Biomedical Engineering, Chemistry, Mechanical Engineering, Electrical Engineering and Computer Science, Center for Bio-Integrated Electronics, Simpson Querrey Institute for Nano/Biotechnology, Northwestern University, Evanston, IL, 60208, USA

ARTICLE INFO

Article history:

Received 24 February 2020

Received in revised form 30 May 2020

Accepted 7 June 2020

Available online 10 June 2020

Keywords:

Shape memory polymers

Kirigami structures

Mechanical cycling

Guided assembly

ABSTRACT

The assembly of three dimensional (3D) structures through compressive buckling of 2D precursors can serve as a promising and robust tool to realize different classes of advanced materials in a broad range of applications with complex geometries and a span of length scales from sub-micron to macro scales. In this study, a shape memory polymer (SMP) material was used as the precursor to form different configurations of 3D kirigami microstructures. 3D SMP structures can serve in a wide range of applications, such as biomedical and aerospace, which require a level of robustness and compliance. To this end, the mechanical response of assembled 3D buckled kirigami structures were investigated through mechanical cyclic and single loading compression at room and elevated temperatures, respectively. The experiments at room temperature were performed to examine the mechanical resilience and stability of the structures upon repeated loading. The load bearing capacity, resiliency, and stability under deformation were shown to be largely affected by their structural shape. In-situ scanning electron microscopy experiments at elevated temperatures demonstrated the outstanding shape memory behavior by full recovery to their original shape, without any structural damage or fracture. Computational modeling supports the experimental findings and contributes to the understanding of deformation and fracture of the structures.

© 2020 Elsevier Ltd. All rights reserved.

1. Introduction

Multiscale and three dimensional (3D) structures of biological materials with multifunctional properties have been utilized as a design route in many research studies to prepare bioinspired human-made materials and devices, with similar multifunctionality and integrity to biomaterials [1,2]. Such 3D structures with various shapes, configurations, and scales have been realized in applications, such as electronic systems [3–5], biomedical devices [6–8], energy storage [9,10], metamaterials [11,12], functional scaffolds for tissue engineering [13], and others [14,15]. Different fabrication techniques, including 3D printing [16], two-photon/multiphoton lithography [17,18], and strain-induced

bending/folding [19] have been developed to form various 3D structures. Each technique has its limitations and constraints, such as material compatibility and accessible feature sizes and geometries [15,20].

Of these techniques, compressive buckling can serve as a strong tool in the assembly of 3D structures with different materials, geometries, and length scales. In this technique, the non-bonded regions of the 2D precursors on a prestrained elastomer substrate transform into a deterministically controlled 3D structure, in a reversible manner through compressive forces, induced upon the release of the prestrained elastomer [21]. Such structures are referred to as kirigami microstructures. Maintaining the 3D design shape upon the removal of prestrain requires the structure to stay on the assembly elastomer substrate. However, there are practical applications that require operating in a condition that is not compatible with elastomer substrates, such as elevated temperatures, as in templates for materials growth, or

* Corresponding author.

E-mail address: apolycarpou@tamu.edu (A.A. Polycarpou).

¹ Corresponding author for modeling work.

applications which demand a freestanding structure in isolated forms, as in micro-robotics [13]. The freestanding 3D structure can be realized through shape fixation and memory effect using shape memory polymer (SMP) [13,22]. The implementation of 3D SMP-based structures provides the ability to recover from severe deformation and also enables programmable shape changes.

Although different 3D SMP structures have been fabricated, their mechanical response to applied load, and their reversibility is unknown. Past experimental investigations were confined to qualitative methods and not direct mechanical measurements [22,23]. The deformation and mechanical cycling of various configurations of 3D polymer-based kirigami structures were investigated using in-situ compression inside a scanning electron microscope (SEM) [24,25]. The structures were found to be highly resilient upon deformation up to 100% compression and achieved stable hysteresis during cyclic loading. In another study, the effect of different structural defects was investigated under cyclic loading. Similar to non-defective structures, the defective structures also achieved stable hysteresis with steady-state mechanical behavior [26]. Herein, we perform in-situ cyclic compression of 3D SMP structures using an indenter equipped with a flat punch probe. Load–displacement responses, including cyclic loading were measured in-situ at room temperature (RT, 23 °C). Also, in-situ compression experiments inside an SEM were performed to directly observe the shape recovery of the structures after the removal of the stress, at elevated temperature. The experiments were initiated with heating the structures above their glass transition temperature (T_g) by 15 °C, followed by compressing the structures to 30% of their initial height. The structures fully recovered to their initial state upon reheating.

2. Materials and methods

2.1. Fabrication of the structures

Fig. S1 (supplementary material) is a schematic representation of the fabrication process. Fabrication of the 3D SMP structures started with spin coating a thin layer of poly(4-styrenesulfonic acid) as a water-soluble sacrificial layer on a silicon wafer. Spin casting formed the 2D precursors of the SMP, composed of epoxy monomer E44 and curing agent poly(propylene glycol) bis(2-aminopropyl ether) (Jeffamine D-230) mixed with a mass ratio of 44:23. The samples were cured in a furnace for 1 h at 110 °C. A lithographically patterned thin metal layer composed of 10 nm chromium (Cr) and 50 nm gold (Au) served as a hard mask for oxygen plasma etching of the SMP. Transfer of the 2D precursors from the silicon wafer to a water-soluble polyvinyl alcohol tape (PVA, 3M Co.) required the removal of the previously formed underlying sacrificial layer on the silicon wafer, which was accomplished by immersion in water. To define the bonding locations, a thin layer of titanium (Ti, 5 nm thick) followed by a thin layer of silicon dioxide (SiO₂, 50 nm thick) were deposited on selective locations of the precursors by using a flexible shadow mask (75 μm thick polyimide film). Before transfer printing the precursors to the stretched silicone elastomer substrate (Dragon Skin; Smooth-On, Easton, PA), the precursors on the PVA tape and the stretched substrate were exposed to ultraviolet ozone treatment to promote the bonding strength by inducing hydroxyl termination. Releasing the prestrained elastomer substrate after dissolving the PVA tape in water induced compressive forces on the 2D shape memory precursors, which enabled the out of plane deformation of the non-bonded regions of the precursors and thus forming the desired 3D kirigami structures.

A schematic representation of the 2D design patterns used in this work, and their corresponding 3D kirigami structures upon release are shown in Fig. S2 (supplementary material). Fig. 1

shows optical microscopy images of the three fabricated structures bonded on the substrate. Three different structures were fabricated, namely a simple quad leg structure 1, an octa-leg 16 bonding sites structure 2, and a hexa-double leg structure 3. The height of the structures was measured from the side view of the optical images, and found to be 510 μm, 260 μm, and 505 μm for structures 1, 2, and 3, respectively. All structures are supported with vertical legs but with different design, height, and number of legs. The structures were initially cyclically compressed to 20 and 30% of their initial height using an instrumented nanoindenter (TI 980, Bruker) equipped with a flat punch probe. Subsequently, structures 2 and 3 were respectively compressed to 20 and 10%, due to breakage and fracture of the structures at higher compression values at RT. Three loading rates of 5, 10, and 25 μm s⁻¹ were selected to study the load rate sensitivity. The experiments at elevated temperature were performed using in-situ SEM compression with an SEM Picoindenter (PI 88, Bruker), equipped with a flat punch probe (100 × 100 μm² square). All structures were compressed to 30% for one loading-unloading cycle.

2.2. Modeling using finite element analysis (FEA)

Modeling was carried out through 3D FEA using the commercial software ABAQUS. The goal was to capture the 2D to 3D transformation through mechanically guided assembly and compare the stress/strain distribution upon compression at room and elevated temperatures. The silicone elastomer substrate (2 mm in thickness) and the precursors (10 μm in thickness) were modeled using eight-node 3D solid elements and four-node shell elements, respectively. Refined meshes were used to ensure computational accuracy. The elastic modulus and Poisson's ratio values of the elastomer substrate were taken to be $E = 166$ kPa and $\nu = 0.49$. To simulate the experiments, the prestrain was modeled to be 70% for structure 1, and 50% for structures 2 and 3. The SMP can be identified as a thermorheological simple polymer whose thermoviscoelastic behavior can be described by a multi-branch rheological model [27]. In this model one equilibrium branch and several thermoviscoelastic nonequilibrium branches are arranged in parallel. Maxwell elements are used in the nonequilibrium branches to represent the stress relaxation behavior of the material [26]. The parameters for equilibrium and nonequilibrium branches are provided in Table S1 (supplementary material). These data were extrapolated from experimental testing of SMP material indirectly. The parameters used to simulate the mechanical behaviors of SMP in ABAQUS were fitting results of SMP's Dynamic Mechanical Analysis (DMA) curve, using equations described in Ref. [28].

3. Results and discussion

3.1. Mechanical cycling (15 cycles) at RT

Fig. 2(a, b) shows the load–displacement curves for cycling of structure 1 at 20 and 30% compression. The structure was consecutively compressed 15 times, and each 5 cycles is termed a set. The curves show two linear regions corresponding to compression of the top rings with linear elastic deformation, followed by a slight buckling in the legs of the structure. The first cycle showed different behavior with a higher hysteresis loop, due to plastic deformation of the structure [25]. The slight plastic deformation is revealed by residual deformation upon removal of the load. The structure maintained minimal and stable hysteresis by increasing the number of cycles. The hysteresis, recovery, and energy dissipation remained the same between each test set. Compressing to 30% of the structure's height showed similar cyclic behavior but with higher load bearing capacity and lower stiffness. According

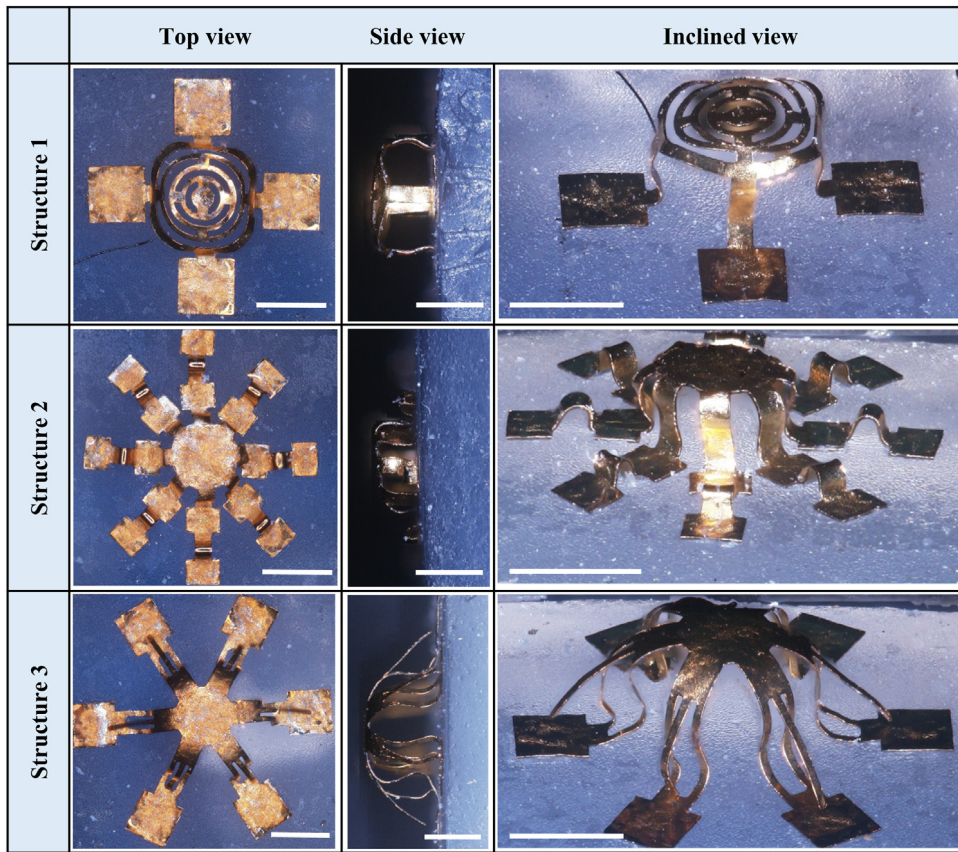


Fig. 1. Optical images of three different 3D kirigami microstructures on elastomer substrate. The scale bars are 500 μm .

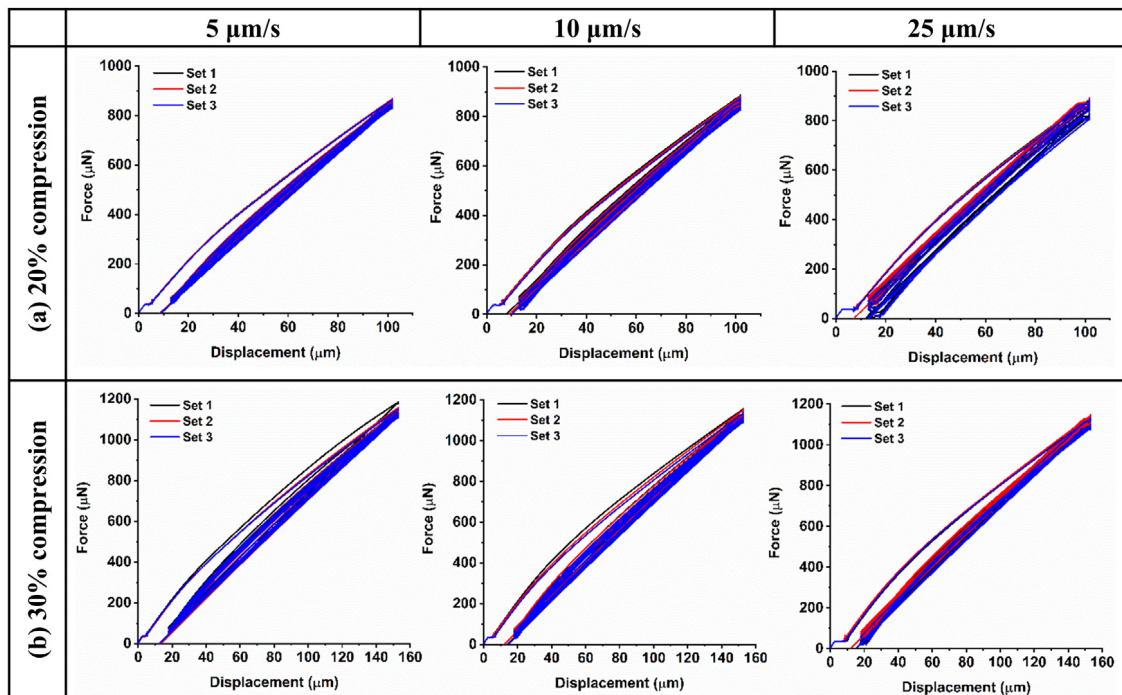


Fig. 2. Load-displacement curves for cycling of structure 1 at (a) 20% compression, (b) 30% compression at different loading rates of 5, 10, and 25 $\mu\text{m}\cdot\text{s}^{-1}$. Set 1 = cycles 1–5, Set 2 = cycles 6–10, Set 3 = cycles 11–15.

to Table S2 (supplementary material), compressing the structure to 30% reduced the stiffness by 12%, compared to 20% compression. The increase of loading rate to 25 $\mu\text{m}\cdot\text{s}^{-1}$ slightly increased

the stiffness by 4% at 20% compression. The structure achieved less hysteresis and stability with increase of the loading rate to 25 $\mu\text{m}\cdot\text{s}^{-1}$.

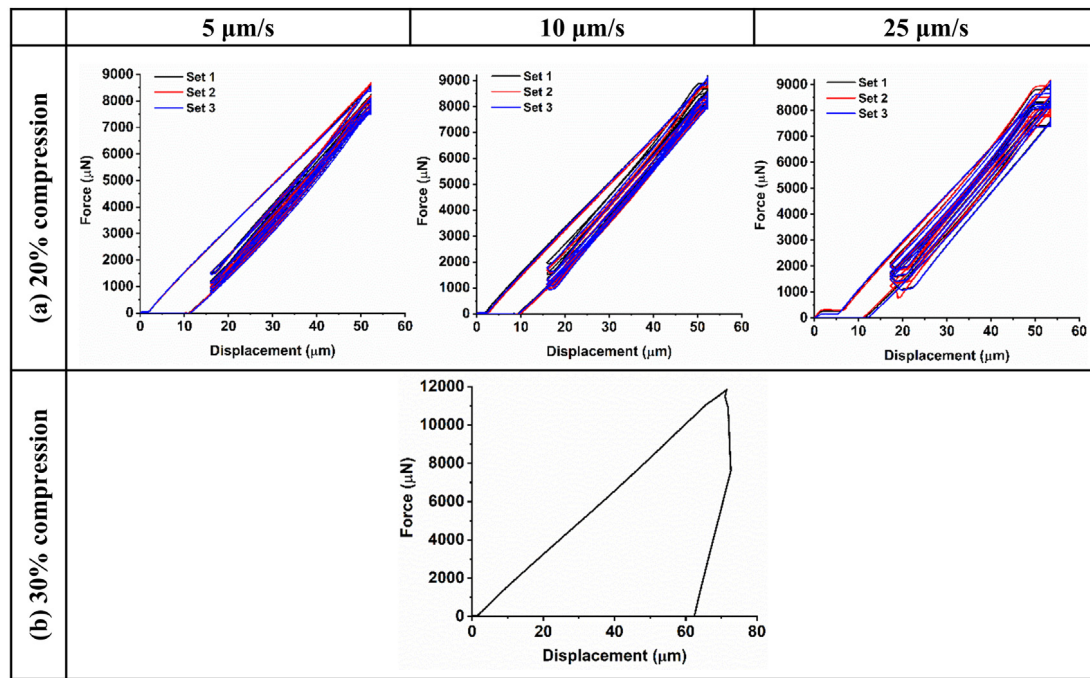


Fig. 3. Load–displacement curves for cycling of structure 2 at (a) 20% compression at different loading rates of 5, 10, and 25 $\mu\text{m}\text{s}^{-1}$, (b) 30% compression at 5 $\mu\text{m}\text{s}^{-1}$, with only one cycle shown since the structure broke, as shown in Fig. S3.

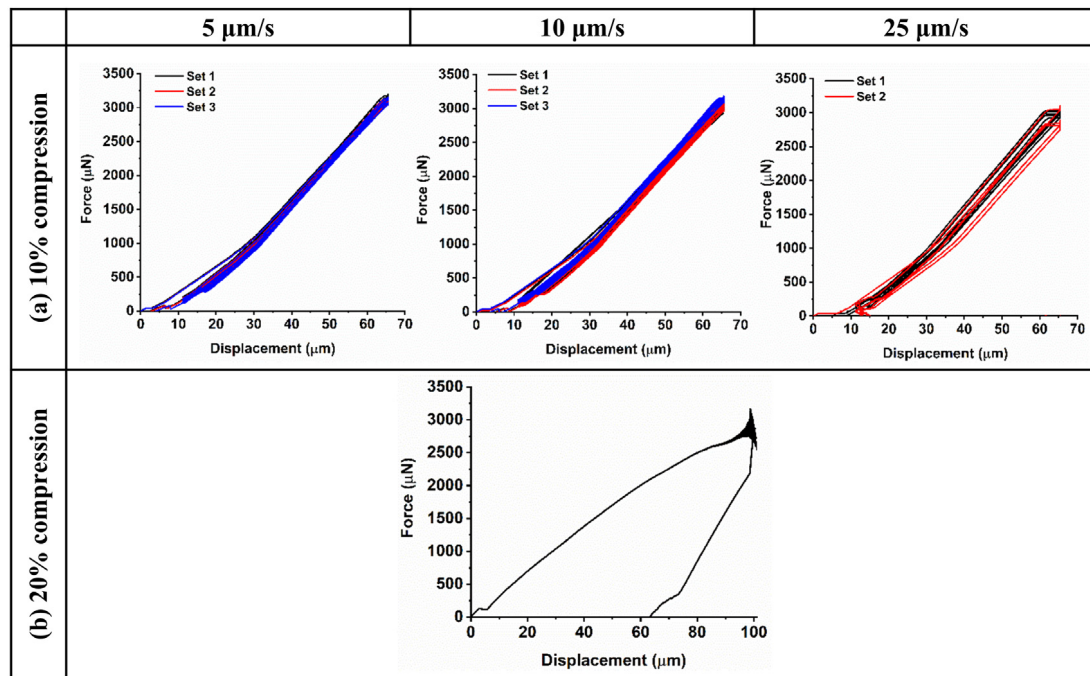


Fig. 4. Load–displacement curves for cycling of structure 3 at (a) 10% compression at different loading rates of 5, 10, and 25 $\mu\text{m}\text{s}^{-1}$, (b) 20% compression at 5 $\mu\text{m}\text{s}^{-1}$, with only one cycle shown since the structure broke, as shown in Fig. S4.

Structure 2 was compressed at the same conditions as structure 1. The load–displacement curves are depicted in Fig. 3(a, b) showing linear elastic deformation at all cycles. Similar to structure 1, the first cycle showed the highest hysteresis, and then exhibited minimal and stable hysteresis. The load bearing capacity increased significantly compared to structure 1. The stiffness remained nearly unchanged at different loading rates (see Table S2). However, the stability reduced by increasing the loading rate to 10 and 25 $\mu\text{m}\text{s}^{-1}$. While the structure could support the load up to 20% compression, cycling to 30% revealed

a different behavior; namely, the structure could not support the load and broke at 70 μm displacement indicating less resilience compared to structure 1. The fracture is captured by a sudden drop in the load–displacement curve. The optical microscopy of the broken sample after the experiment is shown in Fig. S3, indicating the full fracture of two legs from the top membrane.

Fig. 4(a, b) shows the cycling of structure 3 at 10 and 20% compression. Since the structure could not support the load at 20% compression was reduced to 10% of the height. The deformation was dominated by linear elastic behavior at 10% compression.

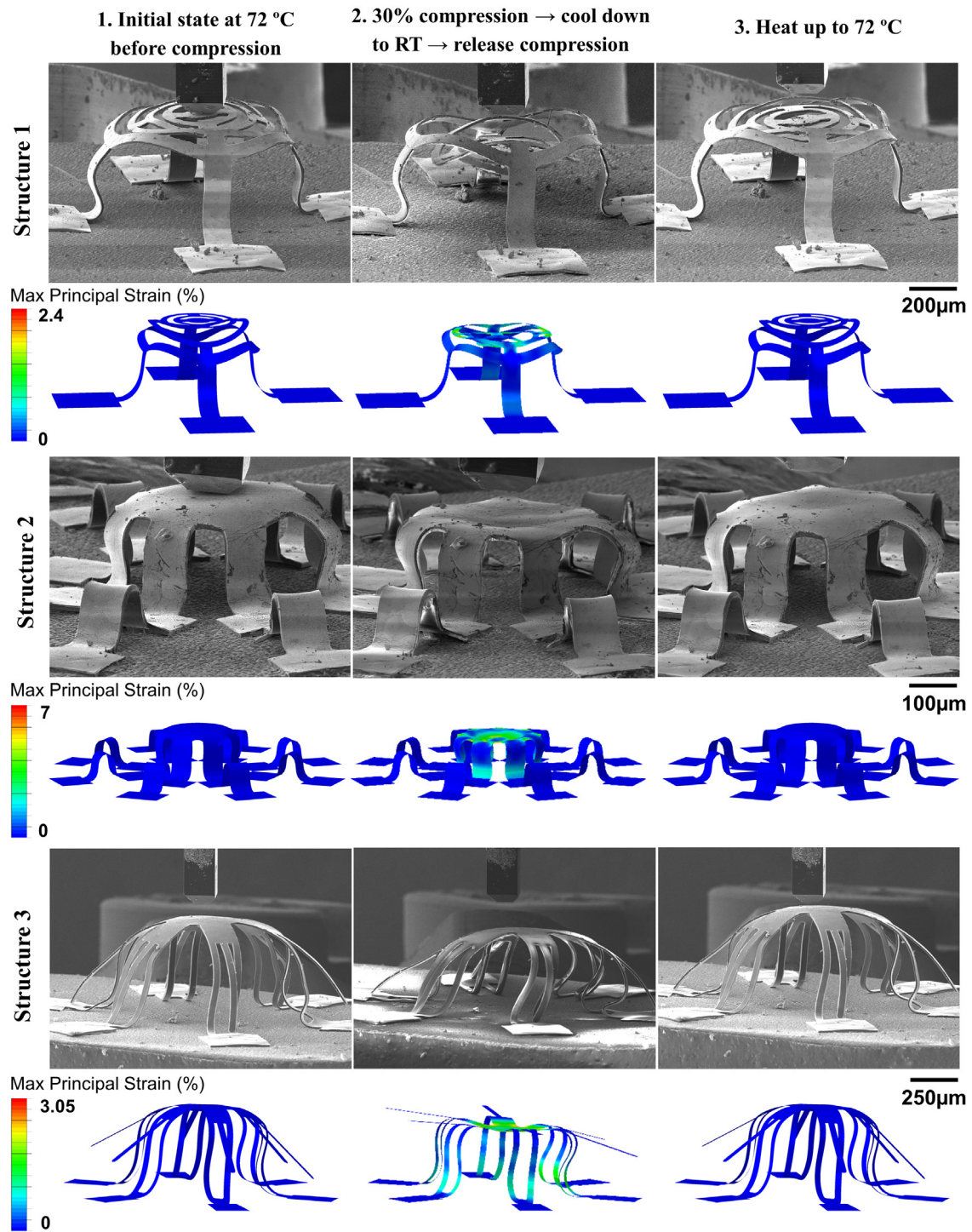


Fig. 5. SEM images and corresponding FEA (% maximum principal strain) for structures 1, 2, and 3 at different steps of the compression process.

Unlike the other structures, the first cycle did not show significant difference in hysteretic loss, compared to the subsequent cycles, especially at the lower loading rate. The structure fully recovered to the initial state upon removal of the load (at 10% compression). The experiments at higher loading rates revealed dependency of hysteresis and stability of the structure to the loading rate. The hysteresis remained stable and without change between each set at the lowest loading rate. Increasing the rate to $10 \mu\text{ms}^{-1}$ imposed a slight shift to the load–displacement curve but with similar hysteresis. At the maximum loading rate, due to unstable behavior, the experiments stopped after set 2. From Table S2,

the increase of loading rate to $25 \mu\text{ms}^{-1}$ slightly increased the stiffness by 4%. The structure could not support the load when compressed to 20% and broke at $90 \mu\text{m}$ displacement, indicating the least resilience among the structures. The compression at 20% was repeated at least three times on the structures with the same 3D geometry, and similar fracture and load–displacement behaviors were observed as in Fig. 4(b). Fig. S4 shows an image of the structure after the experiment, indicating folding and breakage of the legs. The third structure showed the least hysteresis and medium load bearing capacity among the three structures.

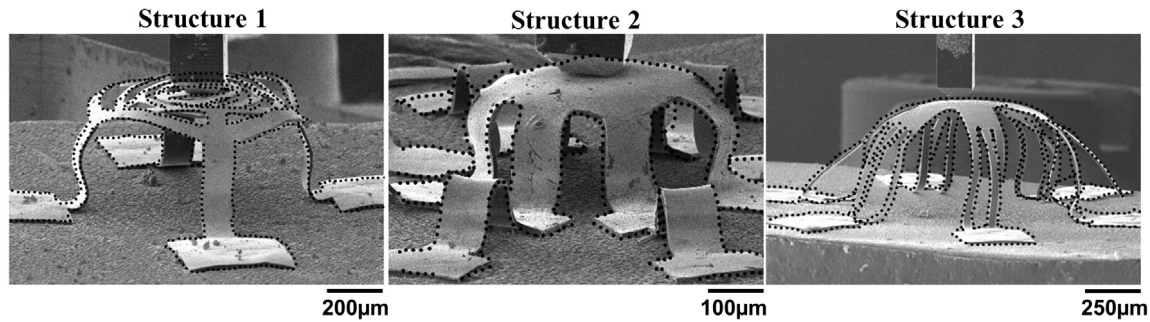


Fig. 6. Superimposed SEM images for structures 1, 2, and 3 before compression and after recovery (the dashed lines show the structure after recovery).

3.2. Shape memory property characterization at elevated temperature

The capacity of SMPs to recover from a fixed deformed shape to their original shape was investigated through in-situ SEM mechanical compression. Exposing the structures to external stimuli such as heat, light, and pH triggers the shape memorization in the material [29]. A second similar exposure after deformation recovers the structure to the original shape. In this work, heating was used as the external stimulus. The experimental process followed three steps:

- Step I: Heating the structures above the glass transition temperature (where $T_g = 57\text{ }^\circ\text{C}$), which triggered high mobility and flexibility in the chains. Upon transition, the structures become soft and the storage modulus changes from 3 GPa to 10 MPa [22];
- Step II: Following heating, the structure was compressed by 30% using a flat punch probe and cooled down to RT, while it was under the applied load. During cooling the chains locked in place and the structures stayed in the deformed shape;
- Step III: Upon removal of the load, the structure was heated again with the same initial heating rate, in which case the structure recovered to its original shape.

Fig. 5 shows a direct comparison of the experimental results and FEA simulations, and the latter gives the strain distribution. The SEM images were taken from all three structures at different steps of the experimental process: (1) image after heating the structures above T_g to $72\text{ }^\circ\text{C}$, (2) image of the structures under 30% compression after cooling down to RT and removal of the flat punch probe from the structures, and (3) image after reheating to $72\text{ }^\circ\text{C}$ showing the recovered structures. The images at step 2 show the deformed structures indicating different deformation mechanisms.

It is clear that at RT (step 2) the structure could maintain the compression induced during temperature above T_g without any constraint. The simulation also demonstrated the deforming, maintaining, and recovering process, with variation of temperature. It is noteworthy that the configuration of the structures used for the simulation (such as the top pads) were slightly different from the experiments, which is attributed to two reasons: First, the observation angle on the simulation was slightly different from the experiment. Second, during manufacturing of the samples, there was deformation between bonding sites and the soft substrate. In the fabricated samples, the bonding sites were not flat, which affected the total configuration, including the legs and the top of the table. In the simulations, non-principal factors such as deformation between bonding sites and elastomer substrate were ignored, which induced minor differences in the configuration, including bulgier pad at the top and flat bonding

sites. The focus of the simulations was on the temperature dependent deformation behavior of the structures, which was in good agreement with the experiments.

Supplementary movies S1–S3 show the in-situ deformation mechanisms upon compression and the recovery after releasing of the load for the three structures. Note that the movies are sped up at different rates during the cycle of heating–cooling–heating. Examining movie S1 (structure 1), the majority of the deformation occurred in the inner rings of the structure with slight buckling on the legs. Recovery followed the same behavior starting from the inner rings and the legs. For structure 2, the majority of the load was supported by the legs causing more resistance to compression, which was also observed by the high load bearing capacity of the structure in the RT experiments. As seen in movie S2 (structure 2), the support of the load by the legs caused deflection on the top membrane leaving a concave shape after cooling. Such mechanism is responsible for failure of the sample during the RT experiments. Furthermore, the FEA results show the strain concentration at the top membrane, in agreement with the experiments. From Fig. S3, the failure at RT was initiated at the top membrane, where the maximum pressure and deflection took place. Similar to structure 1, the recovery started from the membrane and the legs.

A combination of sliding and bending deformation occurred for structure 3 and became larger at higher compression. From movie S3 (structure 3), the legs on the site of the sliding direction experienced twofold bending, while the rest of the legs deformed under onefold bending. As seen in Fig. S4, the failure of the structure at the leg sites during the RT experiments is due to the asymmetrical support of the load, with more severe deformation of the legs in the sliding direction. In addition, the corresponding FEA results indicate similar location where the maximum strain concentration occurred. Recovery followed the same path as loading, starting from recovery of the legs in the sliding direction. Despite the RT experiments, where some of the structures failed, the activation of shape memory effect resulted in full recovery of all three structures. From the superimposed images in Fig. 6, all the structures demonstrated 100% recovery without any structural damages and fracture, indicating their outstanding shape memory behavior.

FEA simulations were carried out to compare the stress/strain distributions at room and elevated temperatures. Fig. 7 and Fig. S5 show the contours of von Mises stress and maximum principal strain, respectively, upon compression to 30%. The compressions at RT have almost the same strain values compared to high temperature, as the structures compressed under similar compression. The von Mises stress increased significantly upon compression at RT as the modulus is higher at RT, compared to elevated temperature. Structure 2 experienced the highest stress among the three structures, which was located at the top membrane and membrane-ribbon connections. Note that this is the same location where fracture occurred at RT experiments

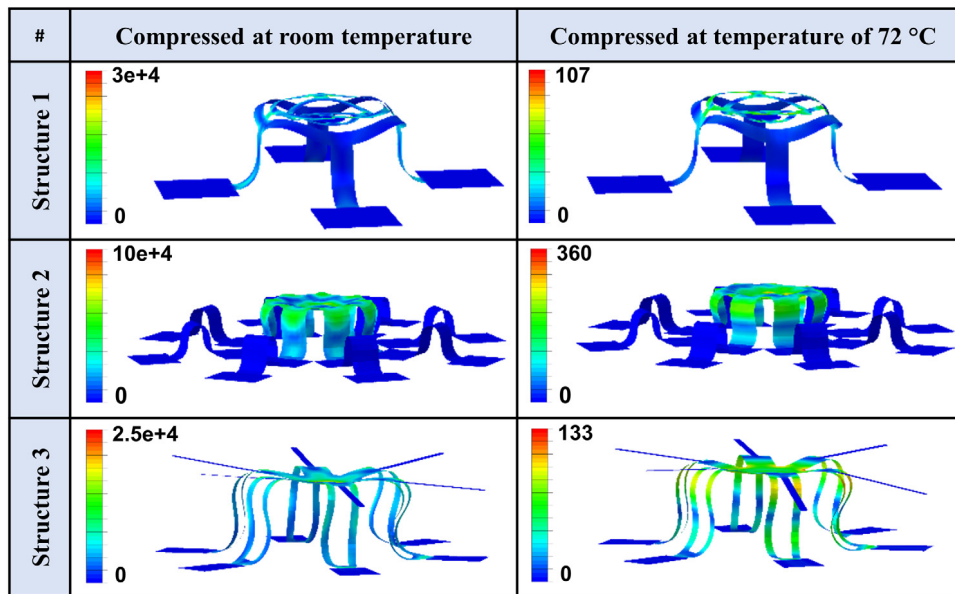


Fig. 7. FEA results showing von Mises stress distributions (MPa) for compression of the structures at RT and high temperature of 72 °C (note that the scales are different for the stress contours).

(see Fig. S3). Structures 1 and 3 showed nearly similar maximum stress values, but different distribution. The maximum stress was located at the membrane-ribbon connections of structure 3, where bending deformation took place and fracture occurred (Fig. S4).

Flexible, robust, and shape-programmable 3D SMP kirigami-inspired structures are promising for different applications, including biomedical devices for tissue repair and vascular stents [30], as well as adaptive and deployable structures in aerospace engineering [31]. In addition, the mechanics-deterministic nature of the 3D buckling technique allows freedom to design and fabricate 3D structures of well-controlled geometries in advanced materials, including combination of SMPs with functional electronics. Although epoxy SMPs are used in this work, the fabrication and characterization techniques developed herein are applicable to SMPs with a wide range of glass transition temperatures (20–300 °C).

4. Conclusion

3D kirigami microstructures were fabricated with different geometrical configurations from epoxy shape memory polymer, using compressive buckling. The mechanical response of the structures was measured at room and elevated temperatures, under cyclic and single compressive loading, respectively. The goal was to evaluate the resilience and stability of the structures upon compression from 20% to 30% of their initial height, and examine and compare their behavior with experiments at elevated temperature with shape memory effect.

The experiments at RT revealed strong dependency of mechanical performance upon deformation (e.g., resilience, load bearing capacity, stiffness, and energy dissipation) to the initial configuration of the structures. The simplest quad-leg structure 1 showed the lowest load bearing capacity and stiffness, but the highest resilience compared to the other more complex structures. The most complex octa-leg 16 bonding sites structure 2, showed the highest load bearing capacity and stiffness but lower stability and higher hysteresis, compared to structure 1. Hexa-double leg structure 3 showed the lowest hysteresis and medium load bearing capacity and stiffness, but the least resilience upon compression, as the sample fractured beyond 10% compression.

The in-situ SEM compression experiments at elevated temperature (above glass transition) demonstrated the shape memory effect in the structures. All structures fully recovered to their initial state after experiments at 30% compression. Unlike the experiments at RT, no structural fracture was observed after the experiments. Modeling using FEA indicated that the fracture of structures 2 and 3 at RT experiments could be attributed to their structural design (with high von Mises stress). Shape memory is an effective way to enhance the performance of these flexible kirigami microstructures upon loading.

Declaration of competing interest

The authors declare that they have no known competing financial interests or personal relationships that could have appeared to influence the work reported in this paper.

Acknowledgments

Partial funding of this study was provided from the Hagler Institute for Advanced Study (HIAS) at Texas A&M University. Kian Bashandeh acknowledges the support of HIAS through the HEEP graduate fellowship program.

Appendix A. Supplementary data

Supplementary material related to this article can be found online at <https://doi.org/10.1016/j.eml.2020.100831>.

References

- [1] K. Liu, L. Jiang, Bio-inspired design of multiscale structures for function integration, *Nano Today* 6 (2011) 155–175, <http://dx.doi.org/10.1016/j.NANTOD.2011.02.002>.
- [2] N. Zhao, Z. Wang, C. Cai, H. Shen, F. Liang, D. Wang, et al., Bioinspired materials: from low to high dimensional structure, *Adv. Mater.* 26 (2014) 6994–7017, <http://dx.doi.org/10.1002/adma.201401718>.
- [3] J.-H. Ahn, H.-S. Kim, K.J. Lee, S. Jeon, S.J. Kang, Y. Sun, et al., Heterogeneous three-dimensional electronics by use of printed semiconductor nanomaterials, *Science* 314 (80-) (2006) 1754–1757, <http://dx.doi.org/10.1126/science.1132394>.

- [4] L. Xu, S.R. Gutbrod, A.P. Bonifas, Y. Su, M.S. Sulkin, N. Lu, et al., 3D multifunctional integumentary membranes for spatiotemporal cardiac measurements and stimulation across the entire epicardium, *Nature Commun.* 5 (2014) 3329, <http://dx.doi.org/10.1038/ncomms4329>.
- [5] Z. Liu, D. Qi, W.R. Leow, J. Yu, M. Xiloyannis, L. Cappello, et al., 3D-structured stretchable strain sensors for out-of-plane force detection, *Adv. Mater.* 30 (2018) 1707285, <http://dx.doi.org/10.1002/adma.201707285>.
- [6] B. Tian, J. Liu, T. Dvir, L. Jin, J.H. Tsui, Q. Qing, et al., Macroporous nanowire nanoelectronic scaffolds for synthetic tissues, *Nat. Mater.* 11 (2012) 986–994, <http://dx.doi.org/10.1038/nmat3404>.
- [7] R. Feiner, L. Engel, S. Fleischer, M. Malki, I. Gal, A. Shapira, et al., Engineered hybrid cardiac patches with multifunctional electronics for online monitoring and regulation of tissue function, *Nat. Mater.* 15 (2016) 679–685, <http://dx.doi.org/10.1038/nmat4590>.
- [8] X. Liu, H. Yuk, S. Lin, G.A. Parada, T.-C. Tang, E. Tham, et al., 3D printing of living responsive materials and devices, *Adv. Mater.* 30 (2018) 1704821, <http://dx.doi.org/10.1002/adma.201704821>.
- [9] Z. Song, T. Ma, R. Tang, Q. Cheng, X. Wang, D. Krishnaraju, et al., Origami lithium-ion batteries, *Nature Commun.* 5 (2014) 3140, <http://dx.doi.org/10.1038/ncomms4140>.
- [10] M. Han, H. Wang, Y. Yang, C. Liang, W. Bai, Z. Yan, et al., Three-dimensional piezoelectric polymer microsystems for vibrational energy harvesting, robotic interfaces and biomedical implants, *Nat. Electron* 2 (2019) 26–35, <http://dx.doi.org/10.1038/s41928-018-0189-7>.
- [11] C.M. Soukoulis, M. Wegener, Past achievements and future challenges in the development of three-dimensional photonic metamaterials, *Nat. Photonics* 5 (2011) 523–530, <http://dx.doi.org/10.1038/nphoton.2011.154>.
- [12] J.T.B. Overvelde, J.C. Weaver, C. Hoberman, K. Bertoldi, Rational design of reconfigurable prismatic architected materials, *Nature* 541 (2017) 347–352, <http://dx.doi.org/10.1038/nature20824>.
- [13] Z. Yan, M. Han, Y. Shi, A. Badea, Y. Yang, A. Kulkarni, et al., Three-dimensional mesostructures as high-temperature growth templates, electronic cellular scaffolds, and self-propelled microrobots, *Proc. Natl. Acad. Sci. USA* 114 (2017) E9455–64, <http://dx.doi.org/10.1073/pnas.1713805114>.
- [14] J.C. Breger, C. Yoon, R. Xiao, H.R. Kwag, M.O. Wang, J.P. Fisher, et al., Self-folding thermo-magnetically responsive soft microgrippers, *ACS Appl. Mater. Interfaces* 7 (2015) 3398–3405, <http://dx.doi.org/10.1021/am508621s>.
- [15] J. Rogers, Y. Huang, O.G. Schmidt, D.H. Gracias, Origami MEMS NEMS, *MRS Bull.* 41 (2016) 123–129, <http://dx.doi.org/10.1557/mrs.2016.2>.
- [16] D. Lin, Q. Nian, B. Deng, S. Jin, Y. Hu, W. Wang, et al., Three-dimensional printing of complex structures: Man made or toward nature? *ACS Nano* 8 (2014) 9710–9715, <http://dx.doi.org/10.1021/nn504894j>.
- [17] J.H. Moon, J. Ford, S. Yang, Fabricating three-dimensional polymeric photonic structures by multi-beam interference lithography, *Polym. Adv. Technol.* 17 (2006) 83–93, <http://dx.doi.org/10.1002/pat.663>.
- [18] M. Farsari, B.N. Chichkov, Two-photon fabrication, *Nat. Photonics* 3 (2009) 450–452, <http://dx.doi.org/10.1038/nphoton.2009.131>.
- [19] X. Zhang, C.L. Pint, M.H. Lee, B.E. Schubert, A. Jamshidi, K. Takei, et al., Optically- and thermally-responsive programmable materials based on carbon nanotube-hydrogel polymer composites, *Nano Lett.* 11 (2011) 3239–3244, <http://dx.doi.org/10.1021/nl201503e>.
- [20] Z. Yan, F. Zhang, F. Liu, M. Han, D. Ou, Y. Liu, et al., Mechanical assembly of complex, 3D mesostructures from releasable multilayers of advanced materials, *Sci. Adv.* 2 (2016) e1601014, <http://dx.doi.org/10.1126/sciadv.1601014>.
- [21] Y. Zhang, Z. Yan, K. Nan, D. Xiao, Y. Liu, H. Luan, et al., A mechanically driven form of kirigami as a route to 3D mesostructures in micro/nanomembranes, *Proc. Natl. Acad. Sci. USA* 112 (2015) 11757–11764, <http://dx.doi.org/10.1073/pnas.1515602112>.
- [22] X. Wang, X. Guo, J. Ye, N. Zheng, P. Kohli, D. Choi, et al., Freestanding 3D mesostructures, functional devices, and shape-programmable systems based on mechanically induced assembly with shape memory polymers, *Adv. Mater.* 31 (2019) 1805615, <http://dx.doi.org/10.1002/adma.201805615>.
- [23] X. Guo, Z. Xu, F. Zhang, X. Wang, Y. Zi, J.A. Rogers, et al., Reprogrammable 3D mesostructures through compressive buckling of thin films with prestrained shape memory polymer, *Acta Mech. Solida Sin.* 31 (2018) 589–598, <http://dx.doi.org/10.1007/s10338-018-0047-1>.
- [24] M. Humood, Y. Shi, M. Han, J. Lefebvre, Z. Yan, M. Pharr, et al., Fabrication and deformation of 3D multilayered kirigami microstructures, *Small* 14 (2018) 1703852, <http://dx.doi.org/10.1002/smll.201703852>.
- [25] M. Humood, J. Lefebvre, Y. Shi, M. Han, C.D. Fincher, M. Pharr, et al., Fabrication and mechanical cycling of polymer microscale architectures for 3D MEMS sensors, *Adv. Eng. Mater.* 21 (2019) 1801254, <http://dx.doi.org/10.1002/adem.201801254>.
- [26] K. Bashandeh, M. Humood, J. Lee, M. Han, Y. Cui, Y. Shi, et al., The effect of defects on the cyclic behavior of polymeric 3D kirigami structures, *Extreme Mech. Lett.* 36 (2020) 100650, <http://dx.doi.org/10.1016/j.eml.2020.100650>.
- [27] K. Yu, Q. Ge, H.J. Qi, Reduced time as a unified parameter determining fixity and free recovery of shape memory polymers, *Nature Commun.* 5 (2014) 3066, <http://dx.doi.org/10.1038/ncomms4066>.
- [28] Z. Ding, C. Yuan, X. Peng, T. Wang, H.J. Qi, M.L. Dunn, Direct 4D printing via active composite materials, *Sci. Adv.* 3 (2017) e1602890, <http://dx.doi.org/10.1126/sciadv.1602890>.
- [29] K.S. Santhosh Kumar, R. Biju, C.P. Reghunadhan Nair, Progress in shape memory epoxy resins, *React. Funct. Polym.* 73 (2013) 421–430, <http://dx.doi.org/10.1016/j.reactfunctpolym.2012.06.009>.
- [30] W. Zhao, L. Liu, F. Zhang, J. Leng, Y. Liu, Shape memory polymers and their composites in biomedical applications, *Mater. Sci. Eng. C* 97 (2019) 864–883, <http://dx.doi.org/10.1016/j.msec.2018.12.054>.
- [31] Y. Liu, H. Du, L. Liu, J. Leng, Shape memory polymers and their composites in aerospace applications: A review, *Smart Mater. Struct.* 23 (2014) 023001, <http://dx.doi.org/10.1088/0964-1726/23/2/023001>.